nature communications

Article

https://doi.org/10.1038/s41467-024-53383-2

Interfering Josephson diode effect in $Ta_2Pd_3Te_5$ asymmetric edge interferometer

Received: 26 November 2023

Accepted: 7 October 2024

Published online: 19 October 2024

Check for updates

Yupeng Li[1,9], Dayu Yan[1,9], Yu Hong[1,2], Haohao Sheng[1,2], Anqi Wang[1,2], Ziwei Dou[1], Xingchen Guo[1,2], Xiaofan Shi[1,2], Zikang Su[1,2], Zhaozheng Lyu[1], Tian Qian[1,3], Guangtong Liu[1,3], Fanming Qu[1,2,3], Kun Jiang[1], Zhijun Wang[1,2], Youguo Shi[1,3] ✉, Zhu-An Xu[4,5,6], Jiangping Hu[1,7], Li Lu[1,2,3] ✉ & Jie Shen[1,3,8] ✉

Edge states in topological systems have attracted great interest due to their robustness and linear dispersions. Here a superconducting-proximitized edge interferometer is engineered on a topological insulator $Ta_2Pd_3Te_5$ with asymmetric edges to realize the interfering Josephson diode effect (JDE), which hosts many advantages, such as the high efficiency as much as 73% at tiny applied magnetic fields with an ultra-low switching power around pico-watt. As an important element to induce such JDE, the second-order harmonic in the current-phase relation is also experimentally confirmed by half-integer Shapiro steps. The interfering JDE is also accompanied by the antisymmetric second harmonic transport, which indicates the corresponding asymmetry in the interferometer, as well as the polarity of JDE. This edge interferometer offers an effective method to enhance the performance of JDE, and boosts great potential applications for future superconducting quantum devices.

The semiconductor diode is a fundamental component in modern electronics due to the non-reciprocal responses[1]. Analogous non-reciprocal charge transport in superconductors - namely superconducting diode effect (SDE) - has great potential for superconducting quantum electronics, since Josephson junctions (JJs) and superconducting quantum interference devices (SQUIDs) have been key components of superconducting quantum devices[2,3]. SDE in the JJs - namely Josephson diode effect (JDE) - and in intrinsic superconductors has been theoretically proposed in various systems with broken time-reversal and inversion symmetries[4–12]. Field-induced and field-free SDE/JDE has been experimentally observed in various superconductors[13–20], supercurrent interferometers[21–24], and other systems[25–29]. Interestingly, asymmetric supercurrent interferometers or SQUIDs with a non-sinusoidal current-phase relation (CPR) provide a good platform to realize JDE (Fig. 1a) with ultra-small magnetic fields and ultra-low power consumption[21,22], both of which are crucial elements for applications at ultra-low temperatures. Moreover, it is quite feasible to promote their efficiency by varying the generic configuration[9], which is compatible with state-of-the-art lithography technology, and integrate them into large-scale superconducting quantum circuits.

Essentially, the appearance of JDE is related to the difference between maximum(I_{c+}) and minimum(I_{c-}) current in the CPR. The conventional CPR is an odd function of superconducting phase difference φ between superconducting leads, entailing a zero supercurrent at $\varphi = 0$, which shifts [meaning $I(\varphi = 0) \neq 0$] when both time-reversal and chiral symmetries are broken[21,30,31]. To achieve JDE, other mechanisms to cause the CPR deviating from standard sinusoidal $I(\varphi) = I_c \sin(\varphi)$ will also be introduced. The characteristics of CPR, which are usually inferred by the interference pattern of SQUIDs and

[1]Beijing National Laboratory for Condensed Matter Physics, Institute of Physics, Chinese Academy of Sciences, Beijing, China. [2]School of Physical Sciences, University of Chinese Academy of Sciences, Beijing, China. [3]Songshan Lake Materials Laboratory, Dongguan, China. [4]School of Physics, Zhejiang University, Hangzhou, China. [5]State Key Laboratory of Silicon and Advanced Semiconductor Materials, Zhejiang University, Hangzhou, China. [6]Hefei National Laboratory, Hefei, China. [7]Kavli Institute of Theoretical Sciences, University of Chinese Academy of Sciences, Beijing, China. [8]Beijing Academy of Quantum Information Sciences, Beijing, China. [9]These authors contributed equally: Yupeng Li, Dayu Yan. ✉e-mail: ygshi@iphy.ac.cn; lilu@iphy.ac.cn; shenjie@iphy.ac.cn

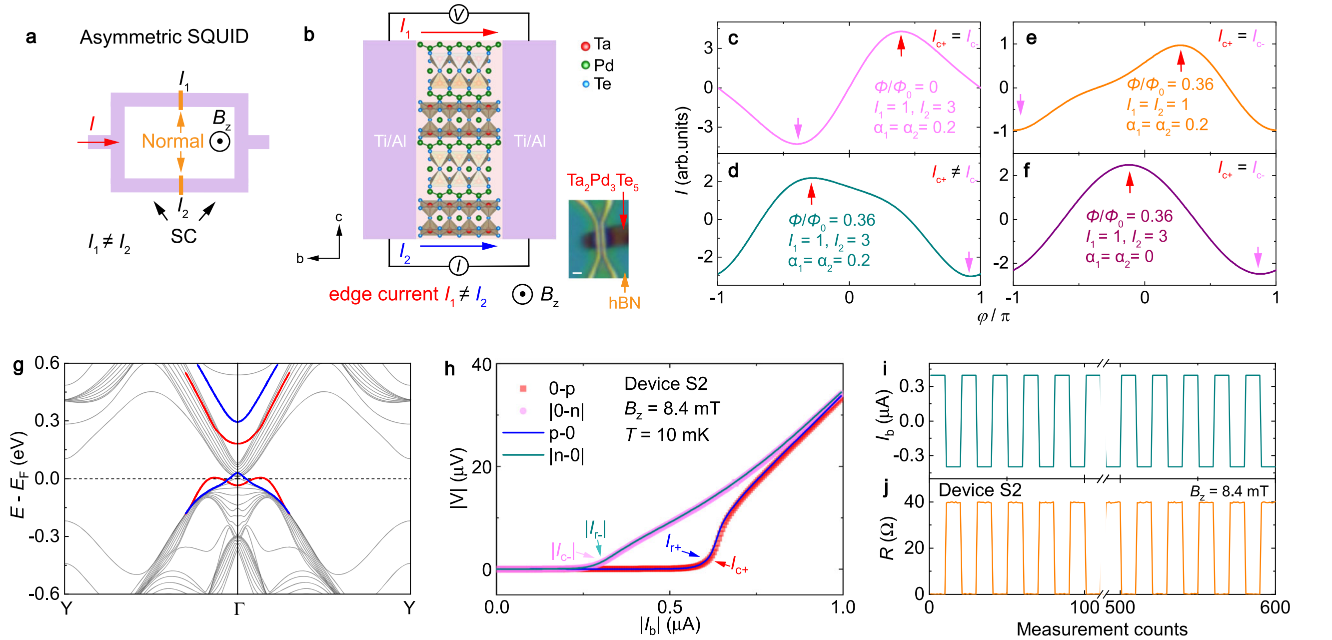

Fig. 1 | Mechanisms for SDE/JDE. **a** JDE in the asymmetric SQUID formed by two asymmetric JJs. **b** An asymmetric SQUID formed by asymmetric edge states in $Ta_2Pd_3Te_5$ JJ and its device configuration. The upper and lower edges are the palladium and tantalum-tellurium atomic chain, respectively. The inset shows the photomicrograph of device S2, and the white scale bar corresponds to 1 μm. **c**–**f** Simulated CPR based on the minimal model. JDE only exists in (**d**) with different supercurrents, a nonzero magnetic field ($\phi/\phi_0 \neq 0$), and higher harmonics in the CPR ($\alpha_n \neq 0$). The red and pink arrows represent the maximum(I_{c+}) and minimum (I_{c-}) current in the CPR, respectively. **g** Band structure of monolayer $Ta_2Pd_3Te_5$. Edge states (blue and red lines) exist near the Fermi level and are marked in the corresponding edges of (**b**). **h** $|I_b| - |V|$ curves for positive and negative current sweep at $B_z = 8.4$ mT. **i, j** Alternating switching between the superconducting and normal states at $B_z = 8.4$ mT and 10 mK in device S2.

the Shapiro steps due to AC Josephson effect, as well as the newly-discovered JDE with non-reciprocal critical current, have been widely harnessed to detect the anomalous superconductivity[32,33], such as proximitized helical/chiral topological edge states. In turn, in a SQUID constructed by two asymmetric edge states of the topological insulator, JDE with an unconventional CPR could be easily realized with highly-tunable efficiency[5] and relatively easy fabrication (Fig. 1b). The relatively small number of edge supercurrent channels, in comparison to the case of bulk states transport, may contribute to the small critical current and power consumption[33,34].

More precisely, the interferometer formed by two asymmetric edge supercurrents (Fig. 1b) can be viewed as a SQUID with two different JJs and induces JDE with requirements similar to the asymmetric SQUID[9] in Fig. 1a. According to Souto et al.[9], a minimal model with n JJs concatenated in an interferometer array is applied to account for the origin of JDE, and the CPR only takes the first and second harmonic contribution into consideration. The current is written as $I(\varphi, \phi/\phi_0) = \sum_1^{n=2} I_n sin(\varphi + 2\pi(n-1)\phi/\phi_0) + \alpha_n I_n sin(2\varphi + 4\pi(n-1)\phi/\phi_0)$ for two-JJs in parallel, where I_n ($\alpha_n I_n$) is the amplitude of the first (second) harmonic content for the nth JJ, α_n is the current coefficient of the higher harmonic, ϕ is the magnetic flux and $\phi_0 = h/2e$ is the magnetic flux quantum. In Fig. 1c–f, the simulations of the CPR using the aforementioned formula serves the purpose of illustrating three key requirements that contribute to the difference between I_{c+} (red arrow) and I_{c-} (pink arrow). First, an external magnetic field ($\phi/\phi_0 \neq 0$) is necessary to break time-reversal symmetry and induce nonzero current at $\varphi = 0$ in the CPR (Fig. 1d–f). Second, the supercurrent of each edge, including all the harmonic contributions, should be different (see Fig. 1d, e and detailed simulations in Supplementary Fig. 2). This condition can be realized by two interfering edge states with different dispersion[5]. It can also be met, for example, by two superconducting quantum point contacts with different transmission coefficients[9], which may be linked to various factors such as different edge states, disorder situations, among others. All of these can cause the different supercurrent of edges in our devices, which is actually quite unique in topological materials. Finally, at least one edge channel should be transmissive so that the CPR acquires a higher harmonic ($\alpha_n \neq 0$)[9,35] (see Fig. 1d, f).

Results

Interfering JDE

In this work, highly efficient JDE, residing in the tilting supercurrent pattern, is reported in a $Ta_2Pd_3Te_5$ edge interferometer at very small B_z and is driven by low power consumption to achieve a highly stable rectification effect. It is also accompanied by fractional Shapiro steps, revealing the higher harmonic contributions of the non-negligible transmission channels. The choice of $Ta_2Pd_3Te_5$ is based on the following reasons: (1) $Ta_2Pd_3Te_5$ is a van der Waals material with quasi-one-dimensional (1D) chains[36] and can be easily mechanically exfoliated. (2) As a 2D topological insulator, where multiple layers could be viewed as simple stacking of monolayers due to very weak inter-layer coupling[37,38], it hosts excitonic insulator states[39–41] and edge states observed by scanning tunneling microscopy[40,42] and transport measurements[38,43]. Notably, owing to the anisotropic bonding energy of 1D chains, the edges possess different atomic chains (Pd and Ta-Te atomic chains), resulting in asymmetric dispersion, as shown by the red and blue lines/arrows in Fig. 1b–g. (3) Superconductivity can be easily achieved in this system through doping or high-pressure techniques[44–46]. Therefore, by proximity effect, the induced supercurrent (Supplementary Fig. 1) carried by edge states of $Ta_2Pd_3Te_5$ can be used to realize an asymmetric SQUID with the interfering JDE.

In Fig. 1h, JDE reaches up to 73% efficiency [$\eta = 2(I_{c+} - |I_{c-}|)/(I_{c+} + |I_{c-}|)$] at an out-of-plane magnetic field $B_z = 8.4$ mT in $|I_b| - |V|$ traces. The measurement is performed in the following sequence: (1) Zero-to-positive current sweep (0-p, red scatters); (2) Positive-to-zero current sweep (p-0, blue line); (3) Zero-to-negative current sweep (0-n, magenta scatters); (4) Negative-to-zero current

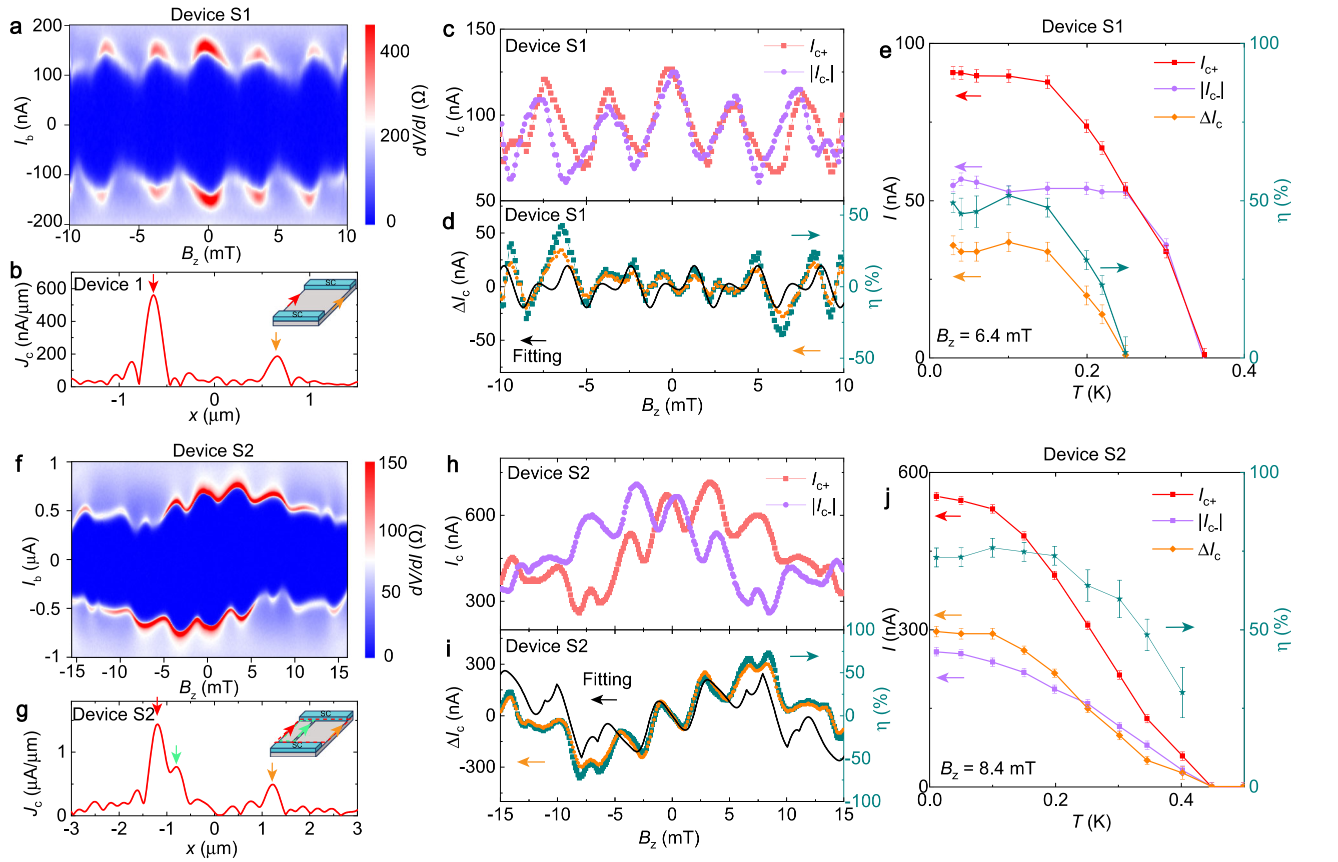

Fig. 2 | Asymmetric Josephson effect and JDE in $Ta_2Pd_3Te_5$ JJs. a SQUID pattern of device S1 at 15 mK. **b** Position-dependent supercurrent density distribution. Inset: A sketch of edge supercurrents-formed JJ. **c** B_z-dependent I_{c+} and $|I_{c-}|$. The switching current I_{c+} and I_{c-} are extracted by ~15% of normal resistance. **d** Non-reciprocal critical current $\Delta I_c = I_{c+} - |I_{c-}|$, Josephson diode efficiency η and fitted ΔI_c (black line) as a function of B_z. **e** Temperature-dependent I_{c+}, I_{c-}, ΔI_c and η for device S1 at $B_z = 6.4$ mT. The error bars primarily stem from the definition of the switching current, which is determined by 15% ± 5% drop of the normal resistance. **f** SQUID pattern of device S2 at 10 mK. **g** Supercurrent density distribution. The inset is a draft of the JJ with three-edge supercurrents. **h** B_z dependence of I_{c+} and $|I_{c-}|$. **i** Oscillating ΔI_c, η and fitted ΔI_c (black line). **j** Temperature-dependent I_{c+}, I_{c-}, ΔI_c and η for device S2 at $B_z = 8.4$ mT. The error bars are obtained by the same method as in (**e**).

sweep (n-0, cyan line). The retrapping current I_{r+} (I_{r-}) and switching current I_{c-} (I_{c+}) are defined during the positive-to-negative (negative-to-positive) current sweep. I_{r+} ($|I_{r-}|$) is nearly the same as I_{c+} ($|I_{c-}|$), suggesting negligible capacitance in the JJ[6,11,25]. Unlike reciprocal transport ($I_{c+} = |I_{c-}|$ and $I_{r+} = |I_{r-}|$), the difference between I_{c+} (I_{r+}) and $|I_{c-}|$ ($|I_{r-}|$) indicates the presence of JDE in this JJ.

The superconducting half-wave rectification is observed at $B_z = 8.4$ mT and 10 mK in Fig. 1i, j. The 'on'/'off' (superconducting/normal) states are switched by alternating current bias ($I_b = \pm 400$ nA). Many cycles of these alternating measurements are conducted over a measurement time exceeding 1.5 h, demonstrating the high stability of this rectification device, which is crucial for its potential applications. Intriguingly, the estimated switching power ($I_b^2 R_N$) reaches the picowatt level (6.4 pW for device S2 with $R_N = 40\,\Omega$, 0.56 pW for device S1 in Supplementary Fig. 1), which is four and eight orders of magnitude smaller than the field-free Josephson diode[25] and another bulk superconducting diode[13], respectively. This power is also close to or even lower than the power of nanowire/nanoflake SDE systems[19,21,47,48] and thin film SDE systems[15,18,49]. The ultra-low switching power in $Ta_2Pd_3Te_5$ Josephson diodes may be attributed to fewer edge supercurrent channels, making it a potential candidate for applications. Nonetheless, further technological advancements are required to optimize the efficiency, magnetic field conditions, and power consumption not only in this Josephson diode but also in other superconducting diodes.

To further study the origin of JDE, we measure the magnetic flux dependence of the JDE in the $Ta_2Pd_3Te_5$ JJ. In Fig. 2a, dV/dI as a function of B_z and I_b displays a SQUID pattern for device S1, suggesting the supercurrent interference of two channels in this JJ. The sawtooth-shaped I_c pattern shows up, usually indicating the involvement of higher harmonic components due to non-negligible transmission channels[50], consistent with findings from Supplementary Note 1. The position-dependent supercurrent density distribution (Fig. 2b) extracted from the SQUID pattern[33] and the estimated enclosed area formed by two interference supercurrents (see Supplementary Note 3 and 9) illustrate the supercurrent mainly originates from edge states of the JJ, confirming the reported edge state in $Ta_2Pd_3Te_5$[38,40,42]. In Fig. 2c, the B_z-dependent I_{c+} and $|I_{c-}|$ extracted from Fig. 2a shows the asymmetric Josephson effect. Several features, such as the large deviation of I_c from zero at half flux quantum in Fig. 2c and JDE in Fig. 2d, indicate the asymmetric edge supercurrent channels in this JJ, as detailed in "Methods" section. Moreover, $\Delta I_c = I_{c+} - |I_{c-}|$ oscillates with B_z (orange curve in Fig. 2d), which can be called interfering JDE and is approximately described by the two-JJs model (black line in Fig. 2d, and see the detail in "Methods" section). This type of JDE has been theoretically predicted in Weyl semimetals with broken inversion symmetry and asymmetric helical edge states[5]. Furthermore, the oscillating Josephson diode efficiency (cyan line in Fig. 2d) shows a maximal efficiency η≈45% at 6.4 mT. It is intriguing that η can reach 10% at $B_z = -0.5$ mT. Also, the required field can be

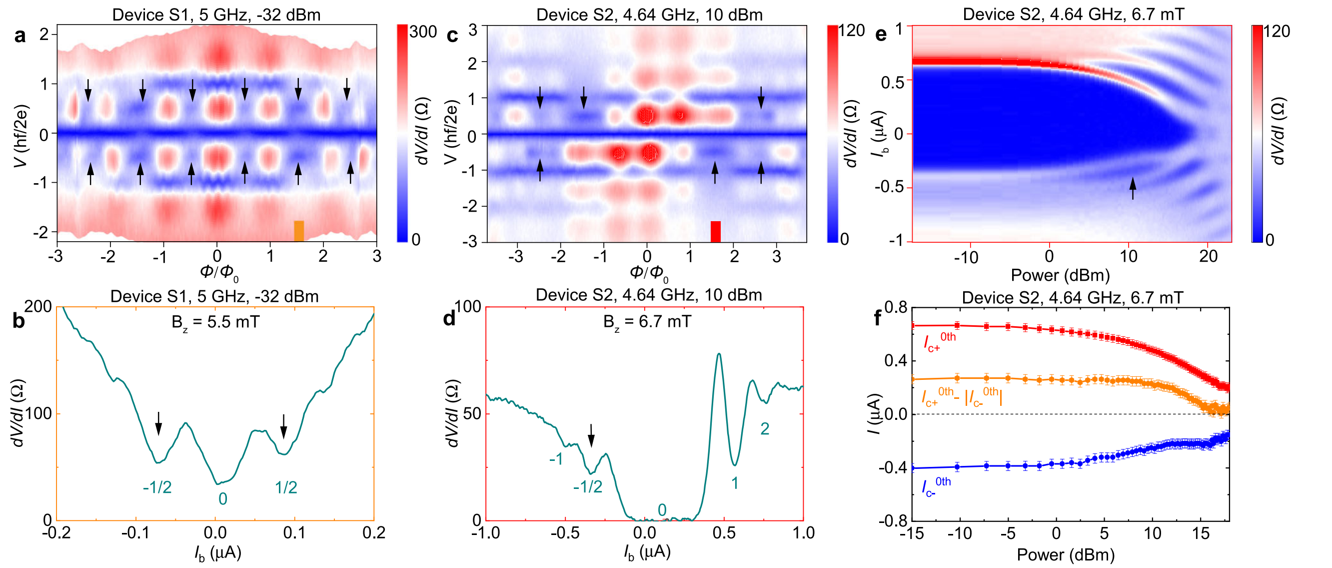

Fig. 3 | Fractional Shapiro steps under microwave in both $Ta_2Pd_3Te_5$ devices. **a** Differential resistance (dV/dI) as a function of voltage characteristics and flux quantum at microwave power = −32 dBm, f = 5 GHz, and 30 mK for device S1. The ±1/2th Shapiro steps are marked by black arrows. **b** dV/dI versus I_b at B_z = 5.5 mT (3/2 ϕ_0). Valleys characterized by half-integer steps are observed clearly. **c** Flux quantum and voltage dependence of dV/dI at microwave power = 10 dBm, f = 4.64 GHz, and 10 mK for device S2. **d** Valleys characterized by the −1/2th Shapiro step at 6.7 mT (3/2 ϕ_0). **e** Microwave power dependence of dV/dI at 4.64 GHz and B_z = 6.7 mT in device S2. The −1/2th Shapiro step is marked by black arrows. **f** Microwave power-dependent non-reciprocal critical current of the 0th Shapiro steps, which is extracted from (**e**). The switching currents here can be determined by peaks in the dV/dI - I_b curve, as shown in Supplementary Fig. 8c, and the error bars primarily originate from the broadening of these peaks.

significantly reduced when the enclosed area of the SQUID loop is increased, which could be easily realized in the experimental setup[21,22].

Having demonstrated the JDE in $Ta_2Pd_3Te_5$ edge interferometer, we now show how to further enhance its efficiency. Interestingly, compared with device S1, the SQUID pattern of device S2 in Fig. 2f reveals two main periods, leading to a more pronounced asymmetry in the pattern (Fig. 2h, i) and an increased efficiency with η_{max} = 73% at 8.4 mT. The enhanced JDE can be explained by three-JJs in parallel. The formation of the middle edge state in the JJ may stem from the ladder-like structure induced by imperfect exfoliation (as indicated by the green arrow in the inset of Fig. 2g and supplementary Fig. 3d), which is a common occurrence during the exfoliation process of 2D flakes[51]. These three supercurrent channels form two sets of interference patterns (corresponding red and green dashed loops in the inset of Fig. 2g), leading to the asymmetric SQUID. The ΔI_c can also be approximately fitted by the three-JJs model (black line in Fig. 2i, and see the detail in "Methods" section). The optimization of η in device S2 (Fig. 2j), compared to device S1 in Fig. 2e, seems to be achieved by increasing the number of JJs in parallel, which is in line with the theoretically predicted method[9].

Here, we examine the main mechanisms to determine which one best fits our data. (1) Magnetism mechanism[20] is initially excluded due to the absence of magnetism in the $Ta_2Pd_3Te_5$ JJ. (2) The Rashba-spin orbital coupling (SOC) mechanism is excluded as it typically requires in-plane magnetic fields, and Ising-SOC is also considered implausible because it is usually found in 2D superconductors[52]. (3) JDE/SDE caused by finite-momentum Cooper pairing generally also needs in-plane magnetic fields[8,14]. The absence of obvious enhancement of the upper critical field under in-plane magnetic fields or the approximate butterfly interference pattern in our JJs[14] (Supplementary Fig. 5) leads to the exclusion of finite-momentum Cooper pairing as a mechanism. (4) Nonlinear capacitance[6,28] is absent in this system due to the symmetric superconducting electrodes and the lack of obvious hysteresis between switching current and retrapping current (Fig. 1h). (5) Self-inductance is also found to be too small to be considered (see Supplementary Note 8). Therefore, the main origin of B_z-induced JDE in the $Ta_2Pd_3Te_5$ edge interferometer is attributed to asymmetric edge supercurrents, as detailed in the "Methods" section.

Fractional Shapiro steps

As discussed above, besides asymmetric edge supercurrents and time-reversal symmetry breaking, the remaining higher harmonic in the CPR is further studied to explain the JDE in our JJs. The Shapiro resonances have been widely used to reveal not only the exotic symmetry of Cooper pairing[32] but also the higher harmonic or non-sinusoidal CPR[9,53]. The Shapiro steps appear in the I–V curve at $V = V_n \equiv nhf/2e$ (n is an integer) when the JJ is irradiated with the microwave. If the nth harmonic contributes to the CPR, m/nth Shapiro steps (m is an integer) will be present[9,53]. In Fig. 3a, fractional Shapiro steps emerge at a microwave frequency of f = 5 GHz, indicating the significant transparency of the JJ (Supplementary Note 1). The ±1/2th Shapiro steps at half flux quantum $(n+1/2)\phi_0$ are marked by black arrows, which is also observed in other works[24,54]. The characteristic dV/dI valleys formed by half-integer steps can be clearly observed at marked positions in Fig. 3b at B_z = 5.5 mT (corresponding to 3/2 ϕ_0). In addition, half-integer Shapiro steps are also observed in device S2 with flux-dependent measurements (f = 4.64 GHz in Fig. 3c, d or 5.02 GHz in Supplementary Fig. 7) and power-dependent measurements at $3\phi_0/2$ (Fig. 3e). These experiments indicate the existence of the second harmonic in the CPR, which is also supported by the rapid suppression observed in temperature-dependent ΔI_c compared with I_c in device S1 (see Fig. 2e), because higher harmonics are quickly suppressed when temperature approaches T_c[55]. The rapid suppression of ΔI_c in device S2 (Fig. 2j) seems less pronounced, possibly because its three-JJs model enhances the diode effect, therefore relatively weakening such suppression. In addition to their applications in Josephson diodes, the JJs with higher harmonics also have potential applications in 0 - π qubits, particularly if the first harmonic in the CPR can be effectively eliminated[56–58].

Furthermore, some features in Fig. 3 require further explanation. First, the disappearance of half-integer Shapiro steps at zero field (Fig. 3a, c) may be attributed to the relatively small contribution of the

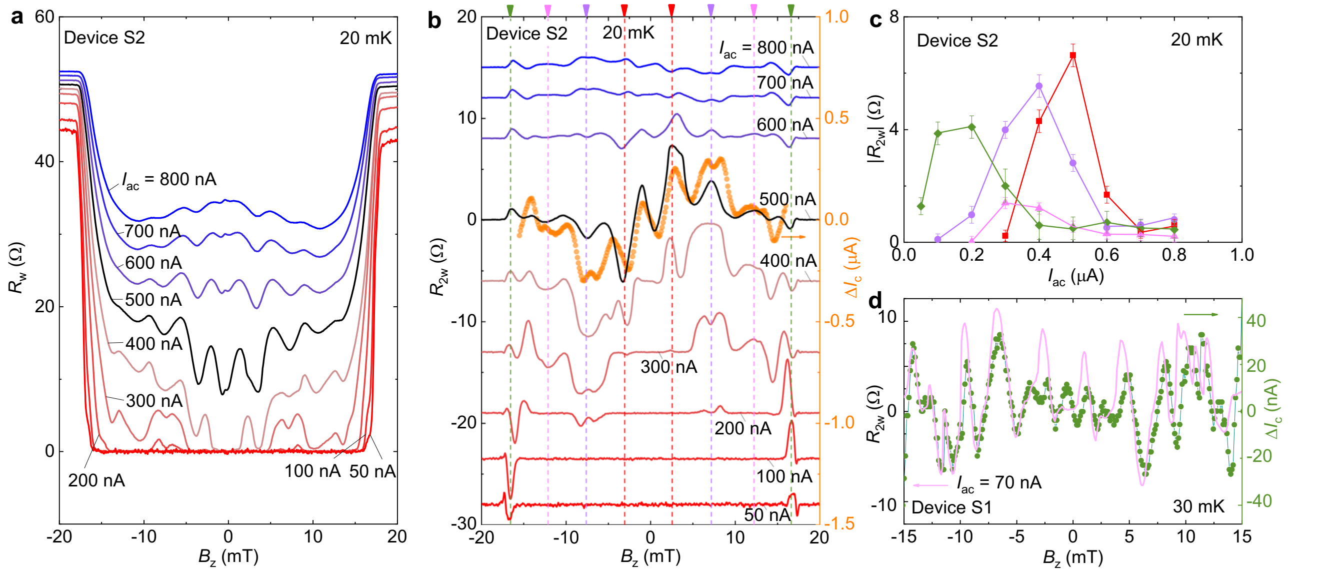

Fig. 4 | Antisymmetric second harmonic transport of $Ta_2Pd_3Te_5$ JJs. a R_w versus B_z at different currents. **b** B_z-dependent R_{2w} at various currents. Typical pairs of antisymmetric peaks (R_{2w}) are marked by dashed lines in matching colors. R_{2w} at 500 nA (black line) shows a similar behavior to ΔI_c (orange line). The green dashed line indicates the regions near the critical fields, while the other dashed line marks the areas near the oscillating peaks or valleys. **c** Typical $|R_{2w}|$ as a function of current at 20 mK for different oscillating peaks. The average $|R_{2w}|$ values are obtained using pairs of antisymmetric peaks near the dashed lines in (**b**). The error bars primarily originate from discrepancies between average $|R_{2w}|$ and the observed values. **d** Antisymmetric R_{2w} and ΔI_c as a function of B_z in device S1. The R_{2w} is measured at I_{ac} = 70 nA.

second harmonic in the CPR and the low microwave frequency[59]. In device S1, a higher microwave frequency is utilized at zero field, and a small signal of half-integer steps appears in Supplementary Fig. 6d–f. No higher frequency is applied to detect half-integer steps at 0 T, considering the limitations of our microwave generator. Second, the integer Shapiro steps at 5.5 mT (3/2 ϕ_0) appear weaker in Fig. 3b (or Supplementary Fig. 6c) compared to those at 0 T in Supplementary Fig. 6b. This is due to the application of a magnetic field at half the flux quantum, causing a reduction in the sharpness of the integer steps because of a decrease in the first harmonic of the CPR. Subsequently, the second harmonic or fractional Shapiro steps become visible at half the flux quantum (Fig. 3a), in agreement with theoretical predictions[9,35] and experimental results[24,54]. Third, in device S2 (Fig. 3c), half-integer steps vanish at $\pm\phi_0/2$ due to the superposition of multiple SQUID patterns, which is slightly different from the single SQUID pattern observed in device S1. In the case of multiple SQUID patterns, the position of destructive interference for the first harmonic differs from that of a single SQUID pattern, leading to a notable contribution from the first harmonic and the absence of half-integer steps at $\pm\phi_0/2$ (see Supplementary Note 6).

The JDE is also studied as a function of microwave power. In Fig. 3f, switching current I_{c+}^{0th} and I_{c-}^{0th} of the 0th Shapiro step are extracted from Fig. 3e. The quantity $\Delta I_c^{0th} = I_{c+}^{0th} - |I_{c-}^{0th}|$ (orange curve, see the detail in Supplementary Fig. 8) displays little variation and gradually decreases with increasing microwave power. This stable observation of the JDE under microwave irradiation represents one of the initial examples of such behavior and is a crucial feature in quantum information applications, where microwaves are commonly utilized[2].

Antisymmetric second harmonic transport

As another type of non-reciprocal behavior, the second harmonic resistance (R_{2w}) is usually measured to characterize magnetochiral anisotropy (MCA)[13,25,60], whose strength is often defined by the coefficient $\gamma = |\frac{2R_{2w}}{R_w BI}|$. MCA typically exhibits antisymmetric behavior in R_{2w} with respect to magnetic fields and is generally used to characterize noncentrosymmetric or chiral features. In normal conductors, MCA is usually a minor effect, generally due to the weak SOC. However, a significant enhancement of MCA is observed in noncentrosymmetric superconductors, potentially offering additional insights into factors such as disparities between the Fermi energy and superconducting gap, the Rashba parameter, and spin-orbit splitting, among other factors[60,61]. Moreover, the antisymmetric oscillations in B-dependent R_{2w} have been observed in an ionic liquid-gated chiral nanotube exhibiting the Little-Parks effect[62], indicating its characteristic chiral symmetry.

Therefore, the second harmonic resistance in our supercurrent interferometer is measured to clarify its asymmetric features. In Fig. 4a, b, the first harmonic resistance (R_w) and R_{2w} of device S2 are measured using lock-in techniques. Below I_{ac} = 100 nA, a typical pair of antisymmetric peaks in R_{2w} is observed at critical fields (near the green dashed line in Fig. 4b). This is consistent with the previously reported antisymmetric peaks of R_{2w} with respect to B in noncentrosymmetric superconductors[13,60], suggesting the existence of asymmetry in our JJ. With increasing I_{ac}, the antisymmetric oscillations in R_{2w} become more pronounced due to the quantum interference of asymmetric edge supercurrents, similar to the behavior observed in chiral nanotubes[62]. At around 500 nA, the oscillating R_{2w} (black line in Fig. 4b) is analogous to the ΔI_c (orange line), and the similar behavior of device S1 can be seen in Fig. 4d (see the detail in Supplementary Note 7). This similarity suggests the antisymmetric oscillations in R_{2w} may be related to the polarity of JDE. At higher I_{ac}, the superconductivity is substantially suppressed and self-heating effects may begin to influence the second harmonic resistance, which is not further analyzed.

In addition, supercurrent interference-induced R_{2w} in our JJs appears more complex. In Fig. 4c, the current-dependent R_{2w} (red, magenta, and violet lines) extracted from the same oscillating peaks below critical fields does not intersect the origin, suggesting deviations from the $R_{2w} = \frac{1}{2}\gamma R_w IB$ formula generally observed in other systems[63–66]. Therefore, although the antisymmetric oscillations in R_{2w} at large I_{ac} display partial antisymmetric features of MCA, the $2R_{2w}/R_w IB$ calculated using the typical formula below the critical field may not accurately describe γ or MCA. The MCA in interference systems appears more complex and requires further investigation.

Discussion

The $Ta_2Pd_3Te_5$ edge interferometer reveals a significant JDE under small out-of-plane magnetic fields. The JDE is accompanied by the enhanced antisymmetric second harmonic transport, which deserves further research. Moreover, the presence of asymmetric Josephson critical current alongside fractional Shapiro steps demonstrates the importance of the higher harmonic content in the JDE. It is noted that power consumption requires attention if SDE/JDE is to be applied at low temperatures in the future, and further optimization is necessary not only regarding mechanism but also in terms of device size. The Josephson diode efficiency can be further enhanced by concatenating interferometer loops. These findings offer a promising approach to exploring JDE with significant diode efficiency, ultra-low switching power at small magnetic fields, and stable JDE under microwave irradiation, rendering them potentially valuable for practical applications.

Methods

Device fabrication

Single crystals $Ta_2Pd_3Te_5$ were prepared by the self-flux method[36]. $Ta_2Pd_3Te_5$ thin films were obtained through mechanical exfoliating bulk samples onto Si substrates with the 280-nm-thick SiO_2 on top, and then coated with PMMA in a glove box at 4000 rpm for 60 s, followed by annealing at 100 °C for 120 s. Multi-terminal electrical contacts were patterned after electron-beam exposure and subsequent development. Ti/Al (5 nm/60 nm) electrodes were deposited after Ar etching in order to remove the oxidized layer. After the lift-off step, the device was coated with hexagonal boron nitride (hBN) to prevent oxidation. The entire fabrication process took place in a nitrogen atmosphere glove box. The rectangular film, with a long side along the *b*-axis of the crystal, was easily obtained due to its quasi-1D nature[38]. The dimensions of device S2 (device S1) are as follows: thickness 37 nm (16 nm), width 1.9 µm (1.3 µm), and length 245 nm (400 nm), respectively.

Transport measurements

The electrical transport measurements were carried out in cryostats (Oxford instruments dilution refrigerator). The DC current bias measurements were applied using a Keithley 2612 current source. Both the first- (R_{ω}) and second harmonic ($R_{2\omega}$) resistance were measured through a standard low-frequency (7–11 Hz) lock-in technique (LI5640, NF Corporation). The phase of the first- and second harmonic signal was set to be 0° and 90°, respectively. The current of the magnet was applied by a Keithley 2400 current source in order to control the magnetic field accurately. Before the measurement, the annealing process with 300 °C for ~10 min was performed to obtain good contacts in the $Ta_2Pd_3Te_5$ JJs. I–V curves were obtained through the numerical integration process and the origin data were all $dV/dI - I_b$ curves.

Transport measurements under microwave radiation

The electrical transport measurements under microwave radiation were carried out using PSG-A Series Signal generator (Agilent E8254A). The main microwave frequency between 4.64 and 5.02 GHz was applied due to the large absorption effect of microwave for devices S1 and S2. The dissipation of the microwave circuit existed during the measurement of device S2, while another microwave circuit for device S1 was good. So the applied power of the microwave was a little large but without inducing obvious thermal effect.

Band structure calculations

The first-principles calculations were carried out based on the density functional theory (DFT) with the projector augmented wave (PAW) method, as implemented in the Vienna ab initio simulation package (VASP)[37]. The generalized gradient approximation (GGA) in the form of the Pardew-Burke-Ernzerhof (PBE) function was employed for the exchange-correlation potential. The kinetic energy cutoff for plane wave expansion was set to 400 eV, and a $1\times9\times1$ **k**-mesh was adopted for the Brillouin zone sampling in the self-consistent process. The thicknesses of the vacuum layer along the x and z axis were set to >20 Å.

Simulations of JDE

A minimal model with n JJs in parallel is used to explain the JDE[9], where only the first and second harmonic contributions in the CPR are considered. The supercurrent is approximatively described as $I(\varphi, \phi/\phi_0) = \sum_1^n I_n sin(\varphi + 2\pi\zeta_n\phi/\phi_0) + \alpha_n I_n sin(2\varphi + 4\pi\zeta_n\phi/\phi_0)$, where ζ_n is the modified ratio and $\zeta_1 = 0$, $\zeta_2 = 1$ ($\zeta_1 = 0$, $\zeta_2 = 1$, $\zeta_3 = 0.23$) for the simulation of our two (three) JJs in parallel. ζ_3 represents the enclosed area ratio of two corresponding SQUID patterns in device S2. Preliminary switching currents for different channels are estimated in both devices without considering the second harmonic contribution, in order to simulate CPR and JDE. For device S1, the parameters used for simulating ΔI_c are: $I_1 = 75$ nA, $I_2 = 15$ nA, $\alpha_1 = 0.3$ and $\alpha_2 = 0.5$, while for device S2, the parameters are: $I_1 = 330$ nA, $I_2 = 120$ nA, $I_3 = 158$ nA, $\alpha_1 = 0.6$, $\alpha_2 = 0.1$ and $\alpha_3 = 0.2$. The simulated ϕ/ϕ_0-dependent ΔI_c can approximatively explain the experimental data in both devices, as shown by black lines in Fig. 2d, i. The slight discrepancy between the simulation and experiment may arise from the omission of higher-order harmonics in the CPR, a reduction in critical current, and a potential variation of α with increasing magnetic field, or other contributing factors.

Asymmetric edge supercurrents

We will discuss edge supercurrents, their asymmetry, and the origin of such asymmetry in our cases, using device S1 as an example. Firstly, the SQUID-like pattern observed in Fig. 2a exhibits several interference features of two edge supercurrent channels, as supported by previous reports[38,40,42]. In this pattern, both the width and amplitude of the center lobe are approximately equal to those of the other lobes. This is obviously contrast to a typical Fraunhofer pattern induced by the bulk transport[33,34], where the width of the center lobe is twice as large as that of the other lobes, while the amplitude of the center lobe is usually significantly larger than that of the other lobes.

Secondly, there are several features supporting asymmetric edge supercurrents in our devices: (1) Without considering the higher harmonics of CPR, we calculated two edge supercurrent channels (I_1 and I_2) from the SQUID pattern in Supplementary Note 3, and in device S1, the ratio between the supercurrents I_1:I_2 is approximately 3.5:1 (I_1:I_2:I_3~6:1:2 for device S2); (2) After considering the second harmonic, from a simple simulation using a two-JJs model in Supplementary Fig. 2e, the deviation of I_c from zero at half flux quantum alone cannot support asymmetric interference channels. However, the coexistence of this deviation and the JDE can support asymmetric supercurrents, as shown in Supplementary Fig. 2d, g, h, and device S1 satisfies this coexistence condition; (3) The position-dependent supercurrent density distribution shows a significantly asymmetric supercurrent distribution. However, it should be noted that such asymmetric supercurrent density distribution can also exist in a symmetric system[33,34] due to the relatively imperfect experimental data.

Finally, the origin of asymmetric edge supercurrents is further discussed: (1) The DFT calculations in Fig. 1g support the existence of asymmetric edge states, which contribute to asymmetric edge supercurrents and JDE[5]; (2) Different transmission coefficients[9] of two edge JJs may also lead to asymmetric edge supercurrents, and can be caused by the different edge disorders, different coupling with the Al contacts, and other factors. Such conditions were not intentionally controlled in our devices.

Discussion of switching power

From a practical perspective, the power consumption of devices should be carefully considered at low temperatures. Although the current cooling power of commercial dilution refrigerators generally reaches the microwatt level at 10 mK[67], a Joule excitation power higher than a picowatt (or nanowatt) may raise the temperature of the device or sensor above 10 mK (or 100 mK) when the mixing chamber is kept at 10 mK[68,69]. The self-heating effect is sometimes noticeable and can also be applied. For example, a microheater with a power output of a few picowatts can generate a temperature gradient as large as several millikelvins per micron and can be further used to conduct Seebeck or Nernst effect measurements in 2D devices at millikelvin base temperatures[70]. Therefore, ultra-low power consumption is essential not only for basic measurements but also for applications in large-scale superconducting quantum circuits, which need ultra-low temperatures to enhance the precision of quantum state measurements.

The edge-induced JDE in $Ta_2Pd_3Te_5$ may offer distinct advantages in terms of power consumption. The edges of the topological system exhibit a low number of conducting channels compared to bulk states transport. This characteristic can result in a lower critical current and reduced power consumption[33,34].

Data availability

All relevant data are available from the authors. The data can also be found at the following link (https://doi.org/10.6084/m9.figshare.26539759).

Code availability

DFT calculations can be reproduced using standard VASP packages. Simulations of JDE are fully described. The codes used in this study are available from the authors upon request.

References

1. Shockley, W. The theory of p-n junctions in semiconductors and p-n junction transistors. *Bell Syst. Tech. J.* **28**, 435–489 (1949).
2. Yu, Y., Han, S., Chu, X., Chu, S.-I. & Wang, Z. Coherent temporal oscillations of macroscopic quantum states in a Josephson junction. *Science* **296**, 889–892 (2002).
3. Ioffe, L. B., Geshkenbein, V. B., Feigel'Man, M. V., Fauchère, A. L. & Blatter, G. Environmentally decoupled sds-wave Josephson junctions for quantum computing. *Nature* **398**, 679–681 (1999).
4. Hu, J., Wu, C. & Dai, X. Proposed design of a Josephson diode. *Phys. Rev. Lett.* **99**, 067004 (2007).
5. Chen, C.-Z. et al. Asymmetric Josephson effect in inversion symmetry breaking topological materials. *Phys. Rev. B* **98**, 075430 (2018).
6. Misaki, K. & Nagaosa, N. Theory of the nonreciprocal Josephson effect. *Phys. Rev. B* **103**, 245302 (2021).
7. Daido, A., Ikeda, Y. & Yanase, Y. Intrinsic superconducting diode effect. *Phys. Rev. Lett.* **128**, 037001 (2022).
8. Yuan, N. F. Q. & Fu, L. Supercurrent diode effect and finite-momentum superconductors. *Proc. Natl Acad. Sci. USA* **119**, e2119548119 (2022).
9. Souto, R. S., Leijnse, M. & Schrade, C. Josephson diode effect in supercurrent interferometers. *Phys. Rev. Lett.* **129**, 267702 (2022).
10. Davydova, M., Prembabu, S. & Fu, L. Universal Josephson diode effect. *Sci. Adv.* **8**, eabo0309 (2022).
11. Zhang, Y., Gu, Y., Li, P., Hu, J. & Jiang, K. General theory of Josephson diodes. *Phys. Rev. X* **12**, 041013 (2022).
12. He, J. J., Tanaka, Y. & Nagaosa, N. A phenomenological theory of superconductor diodes. *New J.Phys.* **24**, 053014 (2022).
13. Ando, F. et al. Observation of superconducting diode effect. *Nature* **584**, 373–376 (2020).
14. Pal, B. et al. Josephson diode effect from Cooper pair momentum in a topological semimetal. *Nat. Phys.* **18**, 1228–1233 (2022).
15. Lin, J.-X. et al. Zero-field superconducting diode effect in small-twist-angle trilayer graphene. *Nat. Phys.* **18**, 1221–1227 (2022).
16. Jeon, K.-R. et al. Zero-field polarity-reversible Josephson supercurrent diodes enabled by a proximity-magnetized Pt barrier. *Nat. Mater.* **21**, 1008–1013 (2022).
17. Bauriedl, L. et al. Supercurrent diode effect and magnetochiral anisotropy in few-layer $NbSe_2$. *Nat. Commom.* **13**, 4266 (2022).
18. Díez-Mérida, J. et al. Symmetry-broken Josephson junctions and superconducting diodes in magic-angle twisted bilayer graphene. *Nat. Commun.* **14**, 2396 (2023).
19. Turini, B. et al. Josephson diode effect in high-mobility InSb nanoflags. *Nano Lett.* **22**, 8502–8508 (2022).
20. Narita, H. et al. Field-free superconducting diode effect in noncentrosymmetric superconductor/ferromagnet multilayers. *Nat. Nanotechnol.* **17**, 823–828 (2022).
21. Ciaccia, C. et al. Gate tunable Josephson diode in proximitized InAs supercurrent interferometers. *Phys. Rev. Res.* **5**, 033131 (2023).
22. Paolucci, F., De Simoni, G. & Giazotto, F. A gate- and flux-controlled supercurrent diode effect. *Appl. Phys. Lett.* **122**, 042601 (2023).
23. Gupta, M. et al. Gate-tunable superconducting diode effect in a three-terminal Josephson device. *Nat. Commun.* **14**, 3078 (2023).
24. Valentini, M. et al. Parity-conserving Cooper-pair transport and ideal superconducting diode in planar germanium. *Nat. Commun.* **15**, 169 (2024).
25. Wu, H. et al. The field-free Josephson diode in a van der Waals heterostructure. *Nature* **604**, 653–656 (2022).
26. Golod, T. & Krasnov, V. M. Demonstration of a superconducting diode-with-memory, operational at zero magnetic field with switchable nonreciprocity. *Nat. Commun.* **13**, 3658 (2022).
27. Hou, Y. et al. Ubiquitous superconducting diode effect in superconductor thin films. *Phys. Rev. Lett.* **131**, 027001 (2023).
28. Trahms, M. et al. Diode effect in Josephson junctions with a single magnetic atom. *Nature* **615**, 628–633 (2023).
29. Sundaresh, A., Väyrynen, J. I., Lyanda-Geller, Y. & Rokhinson, L. P. Diamagnetic mechanism of critical current non-reciprocity in multilayered superconductors. *Nat. Commun.* **14**, 1628 (2023).
30. Szombati, D. B. et al. Josephson ϕ_0-Junction in nanowire quantum dots. *Nat. Phys.* **12**, 568–572 (2016).
31. Yokoyama, T., Eto, M. & Nazarov, Y. V. Anomalous Josephson effect induced by spin-orbit interaction and Zeeman effect in semiconductor nanowires. *Phys. Rev. B* **89**, 195407 (2014).
32. Wiedenmann, J. et al. 4π-periodic Josephson supercurrent in HgTe-based topological Josephson junctions. *Nat. Commun.* **7**, 10303 (2016).
33. Hart, S. et al. Induced superconductivity in the quantum spin Hall edge. *Nat. Phys.* **10**, 638–643 (2014).
34. Pribiag, V. S. et al. Edge-mode superconductivity in a two-dimensional topological insulator. *Nat. Nanotechnol.* **10**, 593–597 (2015).
35. Fominov, Y. V. & Mikhailov, D. S. Asymmetric higher-harmonic SQUID as a Josephson diode. *Phys. Rev. B* **106**, 134514 (2022).
36. Guo, Z. et al. Quantum spin Hall effect in $Ta_2M_3Te_5$ (M =Pd, Ni). *Phys. Rev. B* **103**, 115145 (2021).
37. Guo, Z., Deng, J., Xie, Y. & Wang, Z. Quadrupole topological insulators in $Ta_2M_3Te_5$ (M = Ni, Pd) monolayers. *npj Quant. Mater.* **7**, 87 (2022).
38. Wang, A. et al. A robust and tunable Luttinger liquid in correlated edge of transition-metal second-order topological insulator $Ta_2Pd_3Te_5$. *Nat. Commun.* **14**, 7647 (2023).
39. Huang, J. et al. Evidence for an excitonic insulator state in $Ta_2Pd_3Te_5$. *Phys. Rev. X* **14**, 011046 (2024).
40. Shafayat Hossain, M. et al. Discovery of a topological exciton insulator with tunable momentum order. Preprint at https://doi.org/10.48550/arXiv.2312.15862 (2023).
41. Zhang, P. et al. Spontaneous gap opening and potential excitonic states in an ideal Dirac semimetal $Ta_2Pd_3Te_5$. *Phys. Rev. X* **14**, 011047 (2024).

42. Wang, X. et al. Observation of topological edge states in the quantum spin Hall insulator $Ta_2Pd_3Te_5$. *Phys. Rev. B* **104**, L241408 (2021).
43. Li, Y. et al. $Ta_2Pd_3Te_5$ topological thermometer. Preprint at https://doi.org/10.48550/arXiv.2406.00959 (2024).
44. Higashihara, N. et al. Superconductivity in $Nb_2Pd_3Te_5$ and chemically-doped $Ta_2Pd_3Te_5$. *J. Phys. Soc. Jpn.* **90**, 063705 (2021).
45. Yu, H. et al. Observation of emergent superconductivity in the quantum spin Hall insulator $Ta_2Pd_3Te_5$ via pressure manipulation. *J. Am. Chem. Soc.* **146**, 3890–3899 (2024).
46. Yang, H. et al. Pressure-induced nontrivial Z_2 band topology and superconductivity in the transition metal chalcogenide $Ta_2Ni_3Te_5$. *Phys. Rev. B* **107**, L020503 (2023).
47. Zhang, B. et al. Evidence of ϕ0-Josephson junction from skewed diffraction patterns in Sn-InSb nanowires. Preprint at https://doi.org/10.48550/arXiv.2212.00199 (2022).
48. Mazur, G. P. et al. The gate-tunable Josephson diode. Preprint at https://doi.org/10.48550/arXiv.2211.14283 (2022).
49. Chiles, J. et al. Nonreciprocal supercurrents in a field-free graphene Josephson triode. *Nano Lett.* **23**, 5257–5263 (2023).
50. Murani, A. et al. Ballistic edge states in Bismuth nanowires revealed by SQUID interferometry. *Nat. Commun.* **8**, 15941 (2017).
51. Shi, Y. et al. Imaging quantum spin Hall edges in monolayer WTe_2. *Sci. Adv.* **5**, eaat8799 (2019).
52. Saito, Y., Nojima, T. & Iwasa, Y. Highly crystalline 2D superconductors. *Nat. Rev. Mater.* **2**, 16094 (2017).
53. Chauvin, M. et al. Superconducting atomic contacts under microwave irradiation. *Phys. Rev. Lett.* **97**, 067006 (2006).
54. Ciaccia, C. et al. Charge-4e supercurrent in a two-dimensional InAs-Al superconductor-semiconductor heterostructure. *Commun. Phys.* **7**, 41 (2024).
55. Baumgartner, C. et al. Supercurrent rectification and magnetochiral effects in symmetric Josephson junctions. *Nat. Nanotechnol.* **17**, 39–44 (2022).
56. Larsen, T. W. et al. Parity-protected superconductor-semiconductor qubit. *Phys. Rev. Lett.* **125**, 056801 (2020).
57. Schrade, C., Marcus, C. M. & Gyenis, A. Protected hybrid superconducting qubit in an array of gate-tunable Josephson interferometers. *PRX Quantum* **3**, 030303 (2022).
58. Maiani, A., Kjaergaard, M. & Schrade, C. Entangling transmons with low-frequency protected superconducting qubits. *PRX Quantum* **3**, 030329 (2022).
59. Raes, B. et al. Fractional shapiro steps in resistively shunted Josephson junctions as a fingerprint of a skewed current-phase relationship. *Phys. Rev. B* **102**, 054507 (2020).
60. Wakatsuki, R. et al. Nonreciprocal charge transport in noncentrosymmetric superconductors. *Sci. Adv.* **3**, e1602390 (2017).
61. Hoshino, S., Wakatsuki, R., Hamamoto, K. & Nagaosa, N. Nonreciprocal charge transport in two-dimensional noncentrosymmetric superconductors. *Phys. Rev. B* **98**, 054510 (2018).
62. Qin, F. et al. Superconductivity in a chiral nanotube. *Nat. Commun.* **8**, 14465 (2017).
63. Itahashi, Y. M. et al. Nonreciprocal transport in gate-induced polar superconductor $SrTiO_3$. *Sci. Adv.* **6**, eaay9120 (2020).
64. Choe, D. et al. Gate-tunable giant nonreciprocal charge transport in noncentrosymmetric oxide interfaces. *Nat. Commun.* **10**, 4510 (2019).
65. Legg, H. F. et al. Giant magnetochiral anisotropy from quantum-confined surface states of topological insulator nanowires. *Nat. Nanotechnol.* **17**, 696–700 (2022).
66. Zhang, E. et al. Nonreciprocal superconducting $NbSe_2$ antenna. *Nat. Commun.* **11**, 5634 (2020).
67. Zu, H., Dai, W. & de Waele, A. T. A. M. Development of dilution refrigerators-a review. *Cryogenics* **121**, 103390 (2022).
68. Myers, S. A., Li, H. & Csáthy, G. A. A ruthenium oxide thermometer for dilution refrigerators operating down to 5 mK. *Cryogenics* **119**, 103367 (2021).
69. Yeager, C. J., Courts, S. S. & Davenport, W. E. Thermal resistance of cryogenic thermometers at ultra-low temperatures. *AIP Conf. Proc.* **47**, 1644–1650 (2002).
70. Song, T. et al. Unconventional superconducting quantum criticality in monolayer WTe_2. *Nat. Phys.* **20**, 269–274 (2024).

Acknowledgements

We thank Jin-Guang Cheng for the deep discussions. This work was supported by the Beijing Nova Program (Grant No. Z211100002121144), the Beijing Natural Science Foundation (Grant No. JQ23022), the National Natural Science Foundation of China (Grant Nos. 92065203, 12174430, U2032204, 11974395, 12188101, U22A6005 and 12404154), the Strategic Priority Research Program of Chinese Academy of Sciences (Grant No. XDB33000000 and XDB33030000), the Ministry of Science and Technology of China (Grants No. 2022YFA1403800), the Synergetic Extreme Condition User Facility (SECUF), the Informatization Plan of Chinese Academy of Sciences (CAS-WX2021SF-0102), the Financial Support from Innovation Program for Quantum Science and Technology (Grant No. 2021ZD0302500), the China Postdoctoral Science Foundation (Grant No. 2021M703462 and 2021TQ0356) and the Center for Materials Genome. A portion of this work was carried out at the Synergetic Extreme Condition User Facility (SECUF).

Author contributions

J.S. and Y.P.L. conceived and designed the experiment. Y.P.L. and Y.H. fabricated devices with the help of A.Q.W., X.C.G., X.F.S., and Z.K.S. Y.P.L. and Y.H. performed the transport measurements, supervised by Z.W.D., Z.Z.L., T.Q., G.T.L, F.M.Q., Z.A.X., L.L., and J.S. D.Y.Y. and Y.G.S. synthesized bulk $Ta_2Pd_3Te_5$ crystals. H.H.S. and Z.J.W. calculated the band structure. J.K. and J.P.H. provided some supports on theoretical modeling. Y.P.L. and J.S. wrote the manuscript, and all authors contributed to the discussion of results and improvement of the manuscript.

Competing interests

The authors declare no competing interests.

Additional information

Supplementary information The online version contains supplementary material available at https://doi.org/10.1038/s41467-024-53383-2.

Correspondence and requests for materials should be addressed to Youguo Shi, Li Lu or Jie Shen.

Peer review information *Nature Communications* thanks Cui-Zu Chang and Nicola Paradiso for their contribution to the peer review of this work. A peer review file is available.

https://doi.org/10.1038/s41467-024-53383-2